Materials Advances

ROYAL SOCIETY OF CHEMISTRY

PAPER

View Article Online
View Journal | View Issue

Open Access Article. Published on 08 September 2025. Downloaded on 3/3/2026 7:36:03 PM.
This article is licensed under a Creative Commons Attribution-NonCommercial 3.0 Unported Licence.

Check for updates

Cite this: *Mater. Adv.*, 2025, **6**, 7526

Mn-doping reveals a thermal gap and natural p-type conductivity in Bi_2O_2Se

Antonín Sojka,[a] Jan Zich,[a] Tomáš Plecháček,[a] Petr Levinský,[b] Jiři Navrátil,[a] Pavlína Ruleová,[a] Stanislav Šlang,[a] Ludvík Beneš,[a] Karel Knížek,[b] Václav Holý[cd] and Čestmír Drašar*[a]

Bi_2O_2Se is a semiconductor that is being intensively studied due to its many extraordinary properties. Since about 2010, research on polycrystals has focused on thermoelectric materials. For the last 10 years, single crystal research has been driven by its quasi 2D structure with unexpectedly high permittivity ($\varepsilon_r \approx 500$), which promotes high electron mobility. Bi_2O_2Se thus outperforms other 2D materials in many parameters. However, the high permittivity is also responsible for the extremely low critical concentration of the metal–insulator transition ($n \approx 10^{15}$ cm^{-3}). Thus, Bi_2O_2Se is so far only available as an n-type semiconductor largely with metal-like properties, although the electron concentration can range over 6 orders of magnitude ($n \approx 10^{15}$–10^{21} cm^{-3}), reportedly due to the very high concentration of selenium vacancies or selenium antisites on the Bi site. In this paper, we consider Mn doping in Bi_2O_2Se, $Bi_{2-x}Mn_xO_2Se$. The Mn doping leads to a decrease in the electron concentration and, for the first time, to a transition of the material to p-type conductivity. A thermal gap ($\approx$ 0.9 eV) can be deduced from the temperature dependence of the electrical conductivity. The p-type transition is related to the interaction of Mn with the defect structure of Bi_2O_2Se. Our experiments suggest that the most abundant defects, besides the Se vacancies V_{Se}, are the substitutional defect Se atom at the Bi site, Se_{Bi} and the O atom at the Se site. From high resolution XRD analysis, we conclude that Mn reduces its concentration and brings the structure to the p-type state. From DFT calculations and magnetic data we infer the substitution of Bi by Mn (Mn_{Bi}, in a high spin state, $\mu \cong 5\mu_B$), although all experiments indicate a very low solubility $n_{Mn} = 2.67 \times 10^{18}$ cm^{-3} based on magnetic data.

Received 26th May 2025,
Accepted 5th September 2025

DOI: 10.1039/d5ma00543d

rsc.li/materials-advances

1. Introduction

Thermoelectric (TE) phenomena allow the direct conversion of heat flux into electrical work and *vice versa*. Thus, a so-called thermoelectric generator can be used for long-term recovery of waste heat as part of the green economy. The conversion efficiency is determined by the thermoelectric parameters of the material, the electrical conductivity σ, the Seebeck coefficient S, and the thermal conductivity κ, which together form a thermoelectric figure of merit $ZT = \sigma S^2 T/\kappa$. Therefore, the search for new low-cost and non-toxic thermoelectric materials with sufficient conversion efficiency is crucial for the future of thermoelectric applications.

In the last 15 years, Bi_2O_2Se in the form of single crystals has attracted attention as a quasi-2D semiconductor with unusual properties, such as a very high electron mobility.[1–10] A number of publications on the TE properties of Bi_2O_2Se in polycrystalline form have shown that it is also a promising material because of its TE properties. The absence of tellurium in Bi_2O_2Se, its low cost and ease of preparation also play an important role. In the last decade, most of the research has focused on the optimization of TE parameters such as electrical conductivity, the Seebeck coefficient and thermal conductivity by doping.[11–28] However, the doped materials have been largely "contaminated" by foreign phases (FPs) as a result of doping. This makes it impossible to determine the true properties of this material, especially since FPs appear to modify the grain boundaries. The situation is further complicated by the high concentration of native defects,[29–31] *e.g.* selenium antisites, Se_{Bi} (Se atom in place of Bi) and selenium vacancies, V_{Se} (empty Se site). This motivated us to conduct further research in order to find out the true properties of this material. To achieve this, we have modified the preparation method to significantly reduce the number of grain boundaries and foreign phases.[32,33] The modified preparation method

[a] *Faculty of Chemical Technology, University of Pardubice, Studentská 573, 53210 Pardubice, Czechia. E-mail: cestmir.drasar@upce.cz*
[b] *FZU – Institute of Physics of the Czech Academy of Sciences, Cukrovarnická 10/112, 16200 Prague 6, Czechia*
[c] *Department of Condensed Matter Physics, Faculty of Mathematics and Physics, Charles University, Ke Karlovu 3, 12116 Praha 2, Czechia*
[d] *Department of Condensed Matter Physics, Masaryk University, Kotlařská 2, 61137 Brno, Czechia*

© 2025 The Author(s). Published by the Royal Society of Chemistry

Open Access Article. Published on 08 September 2025. Downloaded on 3/3/2026 7:36:03 PM.
This article is licensed under a Creative Commons Attribution-NonCommercial 3.0 Unported Licence.

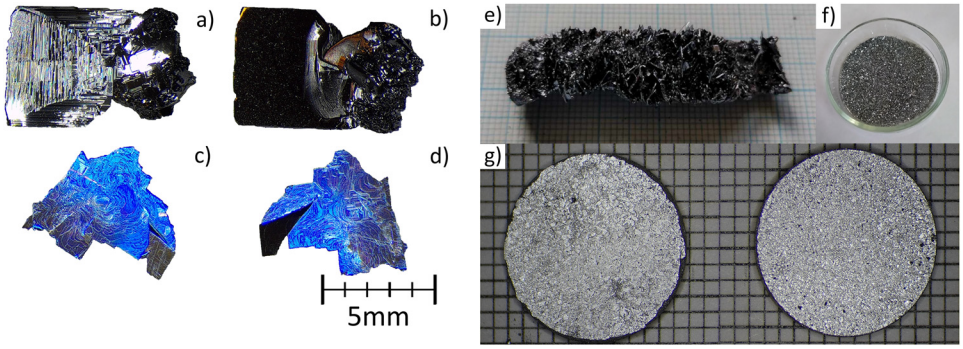

Fig. 1 Comparison of Bi_2O_2Se and $Bi_{1.9}Mn_{0.1}O_2Se$ single crystals. Images (a) and (b) show both sides of typical Bi_2O_2Se single crystals, while images (c) and (d) display both sides of typical $Bi_{1.9}Mn_{0.1}O_2Se$ single crystals. Bi_2O_2Se crystals are thicker with an observable growth pattern on one side, whereas $Bi_{1.9}Mn_{0.1}O_2Se$ crystals are thinner, very brittle, and exhibit a blue appearance likely due to light interference. Image (e) shows the coarse-grained bulk, which consists of a large number of small single crystals. The sieved 35–340 μm fraction is shown in (f). The hot-pressed pellets are shown in (g).

yields a coarse particle fraction ≈ 100 μm, which includes several larger single crystals. Both can be used for characterization (Fig. 1(a)–(d)). Using this approach, we have prepared a series of Mn-doped ($Bi_{2-x}Mn_xO_2Se$, x = 0–0.1) coarse-grained polycrystalline samples and present their properties. For the prepared samples, a thermal energy gap has been measured for the first time, and for the first time a p-type material has been prepared, which is the natural state of strictly stoichiometric Bi_2O_2Se, as indicated by density functional theory (DFT) calculations. Our experiments further suggest that this is due to the reduction/masking of native defects, especially selenium vacancies and antisites, V_{Se} and Se_{Bi}, associated with Mn doping. Although the DFT calculations show similar formation energies for Se_{Bi} and V_{Se}, their concentrations are likely to be strongly dependent on stoichiometry, doping, and preparation conditions. Our results suggest Se-rich rather than Se-poor conditions in our materials. The DFT calculations also indicate that the formation energy of the substitutional oxygen defect at the selenium site (O_{Se}) is very low. We speculate that this point defect may also result from filling the V_{Se} with air oxygen. This defect is electrically inactive but maintains the formal stoichiometry of this compound.

In the initial stage of our study, we prepared a series of polycrystalline Bi_2O_2Se samples doped with various transition metals (Ti, V, Cr, Fe, Co, Ni, Zn, Zr, Nb, Mo, Ta, and W). The goal of these doping series was to explore the solubility and structural stability of Bi_2O_2Se when substituted for the Bi site. However, the results were often inconclusive. We encountered several challenges: the effective doping levels were sometimes below the detection limit; the dopant distribution within the matrix was often uneven; and some samples were poorly compacted or unstable during repeated thermal cycling. These limitations indicated that a more controlled approach was required to reliably understand the role of different dopants. In the subsequent stage, we focused on growing single crystals using an optimized preparation route, as discussed below. We restricted our investigation to a subset of 3d transition metals (Cr, Fe, and Mn) because these elements exhibited the highest solubility in Bi_2O_2Se, and the samples were relatively stable. The Mn-doped series demonstrated a clear tendency toward p-type conductivity; thus, we present it in detail in this work.

2. Experimental

2.1. Synthesis, crystal growth and sample preparation

Bi_2O_2Se samples were prepared by low-temperature synthesis. Bismuth chunks (Sigma Aldrich, 5N) were ground in an MM500nano oscillating mill at 30 Hz for 20 min, selenium shards (Sigma Aldrich, 5N) were hand ground in an agate mortar, and Bi_2O_3 powder (AlfaAesar, 5N) was calcined (decarbonated) at 450 °C for 30 min in an argon stream followed by rapid cooling. These powders were mixed in a stoichiometric ratio in an agate mortar and sealed in a quartz ampoule under pressure $<10^3$ Pa. The ampoule was then placed in a furnace where it was first heated at 0.1 K min^{-1} to 300 °C at which it remained for 1 day and then heated at 1 K min^{-1} to 400 °C, where it remained for 10 days. During this time, the ampoule was rotated at approximately 15 rpm. After cooling at room temperature, the ampoule was placed in a gradient furnace and heated at a rate of 0.1 K min^{-1} to 300 °C, where it was kept for 1 day and then heated at a rate of 1 K min^{-1} to 750 °C (rim)–880 °C (center) where it was held for 14 days. It was slowly cooled to room temperature at a rate of 0.1 K min^{-1} and opened.

This process resulted in a coarse-grained product (Fig. 1e) with crystals up to 6 × 6 mm in size. Large single crystals were hand-picked and used for high resolution (HR) XRD experiments. The bulk of the material consisting of smaller single crystals loosely held together was separated by using sieves of different mesh sizes to remove very small particles and foreign phases. The uncrushed, coarse-grained material (35–340 μm fraction) was used for sample preparation (Fig. 1f). The samples were hot pressed in a silicon nitride (Si_3N_4) die (MTI Corp., USA) with an inner diameter of 12 mm in an Ar atmosphere. The temperature and pressure were gradually increased for 45 min until a temperature of 730 °C and a pressure of 70 MPa were reached. The temperature and pressure were maintained for 3 h, followed by a rapid pressure release. The samples were allowed to cool freely in the press for approximately 3 h. The density of the pressed tablets ranged from 97 to 100% of the theoretical density (Fig. 1g). Samples with a density of less than 97% were excluded from the experiments due to instability with temperature cycling.

Open Access Article. Published on 08 September 2025. Downloaded on 3/3/2026 7:36:03 PM.
This article is licensed under a Creative Commons Attribution-NonCommercial 3.0 Unported Licence.

2.2. High resolution XRD (HRXRD) – structural analysis

The objective of the high-resolution X-ray diffraction (HRXRD) experiments was to confirm the overall crystallographic quality, to reveal the domain structure of the single crystals and to provide the most accurate lattice parameters and lattice position occupancy for a given crystal. Measurements were performed on a Rigaku Smartlab X-ray diffractometer equipped with a 9 kW CuKα rotating anode (45 kV/200 mA). An HRXRD setup with a parabolic multilayer mirror and a 2 × 220 Ge channel monochromator on the primary side and a one-dimensional detector was used to measure the long symmetric $2\theta/\omega$ scans and reciprocal space maps (see SI, Fig. S1).

2.3. DFT calculations – energy of defect formation

Methods based on DFT were applied to calculate electronic structures employing the WIEN2k program.[34] The program uses the full potential linearized augmented plane wave (FP LAPW) method with a dual basis set. In LAPW methods, space is divided into atomic spheres and interstitial region. The radii of the atomic spheres were taken to be 2.325 a.u. for Bi, 1.86 a.u. for O, and 2.325 a.u. for Se and the parameter $R_{mt} \times K_{max}$ was set to 7.5. Calculations of defect energies were performed in a 3 × 3 × 1 supercell with resulting lattice parameters 11.673 × 11.673 × 12.213 Å, which were chosen to achieve similar defect separation in all 3 directions. The size of the supercell, containing a total of 90 atoms, is a compromise between calculation accuracy and computing time requirements and it is the same as used by other authors.[29–31] Since we expected spin-polarized solutions in some cases, all calculations were performed as spin-polarized to enable comparison of the formation energies. The positions of the atoms were optimized for each type of defect. The number of *k*-points in the irreducible part of the Brillouin zone was 172, which is sufficient for the large supercell used. We used the mBJ (modified Becke–Johnson) potential, which is appropriate when the bands around the Fermi surface are predominantly of the s and p character.[35] This potential provides a better description of the band gaps, in particular. However, since mBJ potential is not suitable for calculating forces, it cannot be used for optimization of atom positions. For this purpose and also for comparative calculation of formation energy, we used the GGA (Generalized Gradient Approximation) potential.

2.4. Magnetic properties

Magnetic properties were measured using a MPMS XL 7T SQUID magnetometer (Quantum Design, USA). Magnetization was measured as a function of magnetic field up to ±7 T at various temperatures between 300 and 3 K. DC magnetic susceptibility was measured between 300 K and 3 K in a field of 1 T.

2.5. Transport properties

The electrical conductivity σ was measured by the four-terminal method using an LSR-3 instrument (Linseis, Germany) from 300 to 780 K on round/rectangular hot-pressed samples. The Seebeck coefficient S was measured by the static DC method with the LSR-3; the electrical conductivity was measured simultaneously with the Seebeck coefficient. The measurements were performed in a He atmosphere at 0.1 bar overpressure. The Hall coefficient and the electrical conductivity were measured simultaneously up to 470 K in an argon atmosphere using a home-made cell. The method used an alternating current with a frequency of 1024 Hz and a stationary magnetic field with an induction of 0.4 T. Welded platinum wire voltage contacts and conductive nickel paint (TedPella, Inc.) current contacts were used.

2.6. SEM investigation and EDS analysis

The microstructure study was performed with a scanning electron microscope (SEM) LYRA 3 GMH (Tescan, Czechia). The composition was measured by energy dispersive spectroscopy (EDS) using an Aztec X-Max 20, 5 kV (Oxford Instruments, UK).

3. Results and discussion

3.1. High resolution X-ray diffraction analysis of $Bi_{2-x}Mn_xO_2Se$

Before analyzing the results of the HRXRD experiments, we would like to mention the results based on the powder XRD (PXRD) experiments. These results are summarized in Table S1. Here we highlight only the most significant findings based on the comparison of PXRD and HRXRD. In particular, the Mn-based impurity phase observed in the single crystals is not consistent with the impurity phases found in the sieved fractions. While $MnSe_2$ is most prominent in the larger single crystals (x = 0.04 and 0.1), we observe only traces of Mn_3O_4 in the sieved fractions (35–340 μm) used for compaction for x = 0.1. Unfortunately, we cannot answer this question conclusively. We only refer the reader to the general difficulties associated with the identification of foreign phases in Bi_2O_2Se as discussed in ref. 33. Problems with sample reproducibility and stability are summarized in SI, Section S5.

The Bi_2O_2Se structure corresponds to the structure reported in ref. 36. Fig. S1a and b show the large HRXRD $2\theta/\omega$ scans of the investigated Bi_2O_2Se single crystal samples. We observed a good agreement between the measured, theoretical and fitted diffraction maxima. We used the refinement of the HRXRD data to calculate the concentration of native point defects. Theoretically, Se-vacancies (V_{Se}), the defect oxygen atom on the Se site (antisite O_{Se}), and the defect Se atom on the Bi site (Se_{Bi}) can occur (see Section 3.2 and ref. 30 and 31). Unfortunately, it was not possible to fit the densities of all defect types simultaneously. Therefore, we performed a series of fitting runs assuming the presence of only one defect type. The results are summarized in the SI in Fig. S1a and b. We observed a good agreement between the measured, and fitted diffraction maxima for all defect types considered, slightly smaller fitting residuum was obtained assuming the Se_{Bi} defects (Fig. S1b). This indicates Se-rich growth conditions most likely due to the reaction of Bi_2O_3 with the quartz ampoule.[33] Refinement shows that the crystal composition of the undoped material

 © 2025 The Author(s). Published by the Royal Society of Chemistry

Open Access Article. Published on 08 September 2025. Downloaded on 3/3/2026 7:36:03 PM.
This article is licensed under a Creative Commons Attribution-NonCommercial 3.0 Unported Licence.

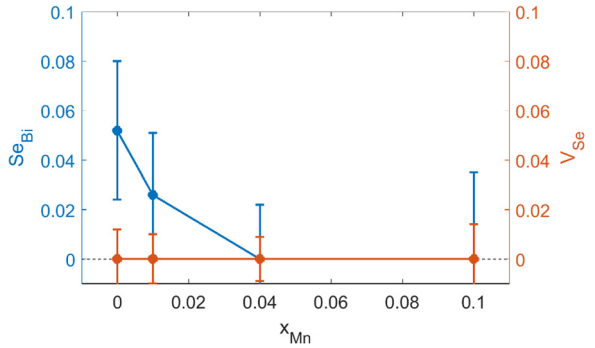

Fig. 2 The density of Se atoms on Bi sites (Se_{Bi}) decreases with increasing Mn content, in contrast to the density of Se vacancies, which remains zero over the doping range (within the error bars) according to HRXRD experiments (fitting details are presented in SI, Section S1).

is approximately $Bi_{1.93}O_2Se_{1.07}$, which is a distinct non-stoichiometry, much higher than that suggested by the EDS analysis (Tables S1a and S2b). Thus, from a concentration point of view, the antisites are likely to be the dominant defect in the studied Bi_2O_2Se. The same refinement procedure gives the concentration of V_{Se} (and thus O_{Se}) close to zero (Fig. S1b). Interestingly, according to HRXRD analysis, Mn doping is associated with a decrease in Se_{Bi}. (see Fig. S1b). The dependence of the Se_{Bi} (V_{Se}) defect concentration on the Mn content is summarized in Fig. 2. Although the results indicate defect healing with respect to Se_{Bi} defects, we must be cautious with our conclusions. In particular, the substitution of Mn for Bi, *i.e.* the formation of Mn_{Bi}, can mimic the formation of Se_{Bi}. The substitution of Mn for Bi produces the same refinement procedure result in terms of atomic position occupation. However, this would contradict the doping process, whereby the concentration of defects decreases with increasing Mn concentration. Thus, we conclude from HRXRD experiments that the solubility of Mn in the Bi_2O_2Se matrix is very low ($x < 0.01$) and most of the Mn segregates as foreign phase(s) at higher nominal concentrations. Although almost invisible in PXRD (Table S1), they are detectable in HRXRD performed on single crystals, where traces of $MnSe_2$ are observed in addition to the low Mn_3O_4 concentration observed in PXRD samples. In conclusion, the decrease in defect concentration largely reflects the decrease in Se_{Bi}, and the solubility of Mn in Bi_2O_2Se is negligible in this sense. The foreign phases largely segregate near the wall of the ampoule, away from the material used for characterization.[33] This conclusion is consistent with the EDS analysis (SI, Section S2) and the magnetic measurements (Section 3.3 below and SI, Section S3), but is inconsistent with the predictions from the DFT calculations below. We use the nominal composition throughout the paper to refer to the samples.

3.2. DFT calculations – band structure and formation energy of defects

The partial density of states (DOS) for doped and undoped stoichiometric materials are shown in Fig. 3.

It shows that undoped stoichiometric Bi_2O_2Se is naturally rather a p-type conductor with the Fermi level close to the valence band edge. This contrasts with the experimental data in the literature reporting only n-type conductivity. We used the mBJ potential, which is suitable for structures with s and p orbitals in the bond and is in better agreement with experiment, at least in terms of the band gap, than the GGA potential. Since mBJ calculates a more accurate electron structure, we also consider the formation energies calculated using the mBJ potential to be more accurate, but we also provide the energies calculated using GGA for comparison. The native point defects with the theoretically lowest formation energy are O_{Se}, V_{Se} and Se_{Bi} (Table 1), in reasonable agreement with the literature.[30,37] The HRXRD experiment above suggests that Se_{Bi} defects are dominant in the present undoped material. Accordingly, the EDS analysis (SI, Section S2) suggests the formation of substitutional defects Se_{Bi} and oxygen on the Se site, O_{Se} in the undoped material.

The partial DOS for the Mn doped material is shown in Fig. 3b. Mn doping shifts the Fermi level deeper into the valence

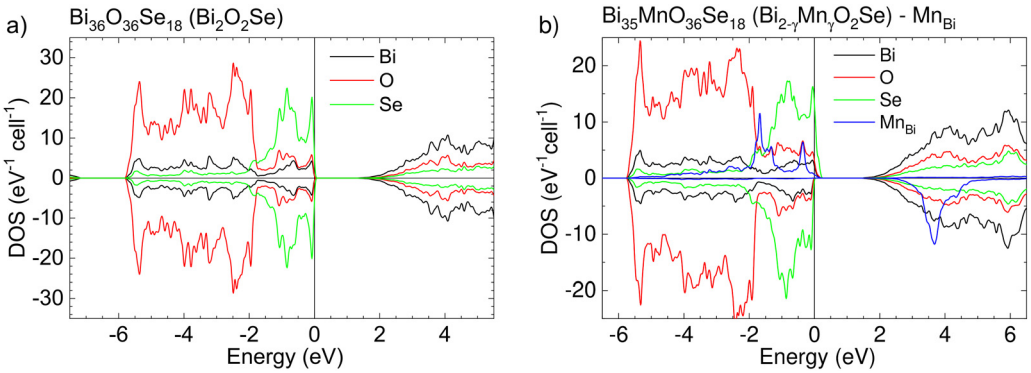

Fig. 3 (a) Partial DOS of undoped stoichiometric Bi_2O_2Se. It shows that Bi_2O_2Se should naturally have p-type conductivity, in line with[38] or in contrast to[39] DFT calculations in the literature. This is in contrast to published experiments which show exclusively n-type conductivity due to the large number of native defects.[2,4,5,29,40] (b) Partial DOS of $Bi_{2-x}Mn_xO_2Se$ for $x = 0.055$. It shows that Mn-doped Bi_2O_2Se should have a distinct p-type conductivity, which is related to the acceptor nature of Mn-based defects, Mn_{Bi} or complex $Mn_{Bi} + V_{Se}$. These defects can be ionized to MnBi1− and $(Mn_{Bi} + V_{Se})^{1-}$ (Table 2) in point defect notation, which is associated with a hole in the valence band. This state is formally equivalent to the Mn^{2+} state with 5 unpaired electrons. The acceptor nature of these defects is translated into an n-type to p-type transition (Section 3.4 below).

Open Access Article. Published on 08 September 2025. Downloaded on 3/3/2026 7:36:03 PM.
This article is licensed under a Creative Commons Attribution-NonCommercial 3.0 Unported Licence.

Table 1 DFT calculated formation energies of native defects for two different potentials. The lowest average formation energy of all calculated point defects in Bi_2O_2Se have the substitutional defect O atom on the Se site, O_{Se}, the substitutional defect Se atom on the Bi site, Se_{Bi} and Se vacancies V_{Se}. The number in bold indicates the defects we consider in the discussion (see SI, Section S4 for details)

Point defect – its designation	Supercell 3 × 3 × 1	Formation energy in eV (mBJ)	Formation energy in eV (GGA)
Bi_2O_2Se – stoichiometric	$Bi_{36}O_{36}Se_{18}$		
See SI, Section S4 for details on Bi vacancies – V_{Bi}	$Bi_{35}O_{36}Se_{18}$	8.93	6.67
O vacancies – V_O	$Bi_{36}O_{35}Se_{18}$	4.40	6.55
Se vacancies – V_{Se}	$Bi_{36}O_{36}Se_{17}$	2.65	4.77
Substitutional defect Se atom on the Bi site – Se_{Bi}	$Bi_{35}O_{36}Se_{19}$	3.27	3.76
Substitutional defect Se atom on the O site – Se_O	$Bi_{36}O_{35}Se_{19}$	4.29	5.25
Substitutional defect O atom on the Se site – O_{Se}	$Bi_{36}O_{37}Se_{17}$	0.99	−0.05
Substitutional defect Se_O + vacancy V_{Se}	$Bi_{36}O_{35}Se_{18}$	6.23	10.1

band consistent with acceptor nature of Mn (Section 3.4). The lowest formation energy of all calculated Mn-based point defects in $Bi_{2-x}Mn_xO_2Se$ has the substitutional defect Mn atom on the Bi site, Mn_{Bi}. The negative formation energy indicates that the Mn_{Bi} can be formed spontaneously for the supercell used, which is in contrast to our experiments. However, it is necessary to consider that the calculated energies correspond to T = 0 K and that a relatively small negative energy with respect to the parent structure does not necessarily mean that this type of substitutional defect will be formed over a wide range of doping levels also at the reaction temperatures. Table 2 summarizes the calculated formation energies of Mn-induced point defects. The EDS analysis (SI, Section S2) shows an "immeasurably" low solubility of Mn in the Bi_2O_2Se structure, and the HRXRD analysis is also consistent with a very low Mn content in the structure. Attempts to grow a pure analog, Mn_2O_2Se, resulted in the formation of a multiphase product but not Mn_2O_2Se (Fig. S8). The DFT calculations disagree also with the magnetic data regarding the spontaneous formation of Mn_{Bi} defects (Section 3.3), but agree in a sense that the Mn_{Bi} defect should be a fully spin polarized Mn^{2+} state (Fig. 3b), which is consistent with ref. 37. More information can be found in SI, Section S4.

In particular, manganese promotes the formation of complex defects Mn_{Bi} + O_{Se} (compare data in Tables 1 and 2). Thus, manganese increases the general tendency of oxygen to fill selenium vacancies, V_{Se}, which are the main donors. In addition, it can inactivate V_{Se} by forming complex defects Mn_{Bi} + V_{Se}. Besides Mn_{Bi} as an acceptor, there are two other mechanisms that contribute to the n-type to p-type crossover associated with depletion/inactivation of V_{Se} as discussed below.

Table 2 does not list the defect Mn atom in the interstitial position, Mn_i. We have tried several interstitial positions for the Mn atom, but the calculations did not converge properly. Thus, we assume that there is simply not enough space for such a defect. In addition, interstitials are usually donors, which is in contrast with the experiment. We also note that lattice parameter c (Fig. S2) does not change with doping indicating that the occurrence of Mn interstitial is unlikely.

3.3. Magnetism and concentration of Mn point defects

All Mn doped samples exhibit significant background diamagnetism (Fig. S3a and b). A fit of the magnetization to the Brillouin function (Fig. 4) gives $S_{spin} \approx 2.4$ and supports the DFT predicted state of the Mn ion close to the Mn^{2+} state with 5 unpaired electrons. The concentration of paramagnetic centers obtained from the fit is $N = 2.67 \times 10^{18}$ cm^{-3}, which corresponds to $x \approx 0.00025$. The Curie–Weiss fit of the magnetic susceptibility χ (Fig. S3b) gives $x \approx 0.00028$ and a Curie–Weiss temperature T_{CW} close to 0 K, proving that the paramagnetic signal comes from Mn ions diluted in the Bi_2O_2Se matrix and not from the observed Mn-based extraneous phases since they all exhibit some form of magnetic interaction.[41,42] Note that the concentration of the Mn^{2+} ions is high enough to play a significant role as an acceptor in the free electron concentration. In fact, this is the only direct evidence we have for the incorporation of Mn into the Bi_2O_2Se as discussed in Section 3.4.

3.4. Transport properties

Fig. 5 shows the Seebeck coefficient and electrical conductivity as a function of temperature for $Bi_{2-x}Mn_xO_2Se$ samples. Both

Table 2 DFT calculated formation energies of Mn defects in Bi_2O_2Se for the different potentials. The lowest average formation energy of all calculated point defects has the substitutional defect Mn atom on the Bi site, Mn_{Bi}. The number in bold indicates the defects we consider in the discussion. See SI, Section S4 for details

Point defect – its designation	Supercell	Formation energy in eV (mBJ)	Formation energy in eV (GGA)
Substitutional defect, Mn atom on the Bi site – Mn_{Bi}	$Bi_{35}O_{36}Se_{18}Mn$	−0.34	−0.28
Substitutional defect, Mn atom on the Se site – Mn_{Se}	$Bi_{36}O_{36}Se_{17}Mn$	1.97	3.66
Complex defect – Mn_{Bi} + V_{Bi}	$Bi_{34}O_{36}Se_{18}Mn$	8.31	6.87
Complex defect – Mn_{Bi} + V_O	$Bi_{35}O_{35}Se_{18}Mn$	3.70	5.59
Complex defect – Mn_{Bi} + V_{Se}	$Bi_{35}O_{36}Se_{17}Mn$	3.69	1.91
Complex defect – Mn_{Bi} + Se_O	$Bi_{35}O_{35}Se_{19}Mn$	4.05	4.96
Complex defect – Mn_{Bi} + Se_O + V_{Se}	$Bi_{35}O_{35}Se_{18}Mn$	6.18	8.56
Complex defect – Mn_{Bi} + Se_{Bi}	$Bi_{34}O_{36}Se_{19}Mn$	2.52	2.80
Complex defect – Mn_{Bi} + O_{Se}	$Bi_{35}O_{37}Se_{17}Mn$	0.76	−0.96

 © 2025 The Author(s). Published by the Royal Society of Chemistry

Open Access Article. Published on 08 September 2025. Downloaded on 3/3/2026 7:36:03 PM.
This article is licensed under a Creative Commons Attribution-NonCommercial 3.0 Unported Licence.

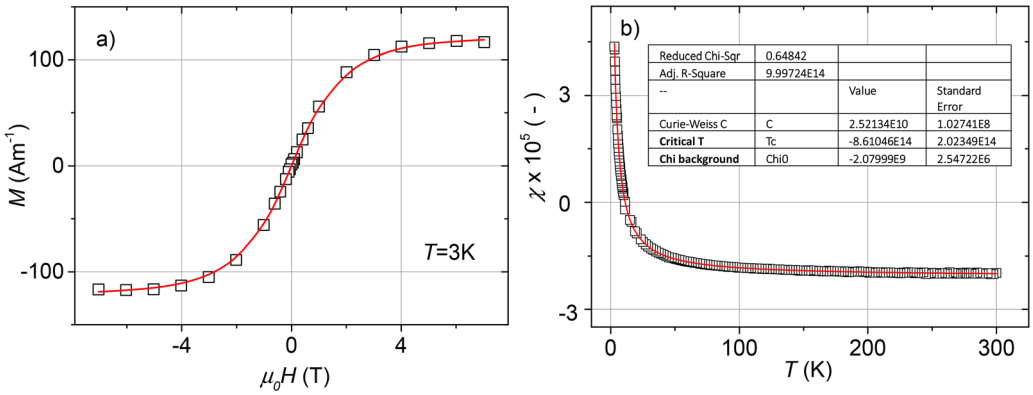

Fig. 4 Magnetic properties of the $Bi_{1.9}Mn_{0.1}O_2Se$ sample (SI units). (a) The paramagnetic part of the magnetization for T = 3 K after subtracting the diamagnetic background (black open squares) can be fitted to the Brillouin function (red solid line). The fit gives S_{spin} = 2.44 ($\mu \cong 5\mu_B$ per Mn atom, in agreement with DFT) and the concentration of paramagnetic centers $N = 2.67 \times 10^{18}$ cm^{-3} corresponding to $x \cong 0.00025$. This is the same value as that obtained from the estimated M_s (Fig. S3a). (b) Magnetic susceptibility as a function of temperature for the H-field parallel to the tetragonal c-axis (perpendicular to the a–b plane). The Curie–Weiss fit (red line) gives an experimental solubility of $x \approx 0.00026$, assuming a magnetic moment of $5\mu_B$ per Mn atom. The Curie–Weiss temperature (T_{CW}) is close to 0 K. The same analysis of the $Bi_{1.96}Mn_{0.04}O_2Se$ sample gives $x \approx 0.00017$, see SI, Section S3.

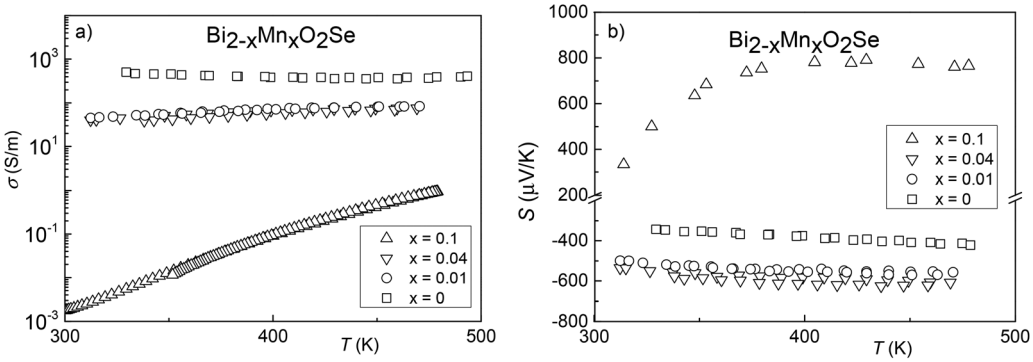

Fig. 5 Electrical conductivity σ (a) and Seebeck coefficient S (b) as a function of temperature for polycrystalline $Bi_{2-x}Mn_xO_2Se$ samples. The experimental data represent temperature dependences in both directions.

reflect the decrease in electron concentration with increasing Mn concentration, which is consistent with the depletion of native donors and the formation of Mn_{Bi} defects. Finally, $Bi_{2-x}Mn_xO_2Se$ reaches the intrinsic state for nominal x = 0.1 and the Seebeck coefficient shows a p-type conductivity. This is the state closer to a stoichiometric undoped material (Fig. 3a). We note that this is the first time that p-type conductivity of Bi_2O_2Se has been observed experimentally. While the x = 0 sample is nearly metallic in the low temperature region, with features of semiconducting behavior in the high temperature region, the $x \geq 0.01$ samples show semiconducting behavior only. The activation energies correspond to point defects energetically located in the band gap (Fig. 6 and Tables 1–3). DFT calculations show the lowest formation energies for O_{Se}, Se_{Bi} and V_{Se}. While Se_{Bi} and O_{Se} have a finite excitation (activation) energy, zero activation energy (resonant states) is reported for V_{Se},[39] which is consistent with our calculations (Fig. S4a and b). The presence of V_{Se} implies that other defects can only show their activation (thermally induced increase in electron concentration or electrical conductivity) only when the background concentration of electrons due to V_{Se} is low enough. Thus, the

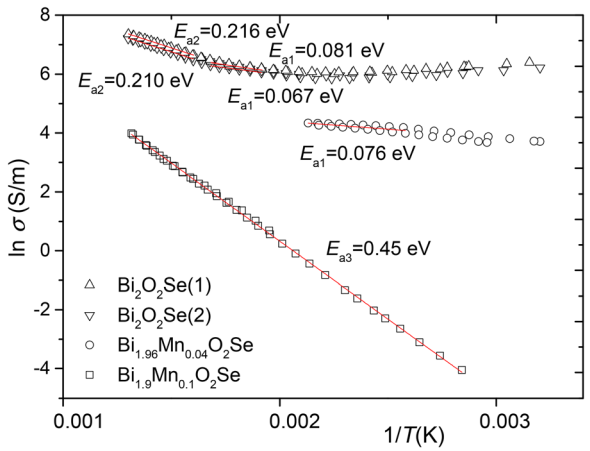

Fig. 6 Analysis of electrical conductivity revealing the activation energies of charge carriers in $Bi_{2-x}Mn_xO_2Se$. The only activation energy of the sample with x = 0.1 corresponds to the fundamental gap observed in ARPES experiments ≈ 0.8 eV.[1] The experimental data represent temperature dependences in both directions.

Open Access Article. Published on 08 September 2025. Downloaded on 3/3/2026 7:36:03 PM.
This article is licensed under a Creative Commons Attribution-NonCommercial 3.0 Unported Licence.

Table 3 Activation energies derived from the Arrhenius plot presented in Fig. 6, compared also with Fig. 7

Activation energy (eV)	E_{a1}	E_{a2}	$E_{a3} = E_g/2$
Bi_2O_2Se (1)	0.081	0.216	—
Bi_2O_2Se (2)	0.067	0.210	—
$Bi_{1,99}Mn_{0,01}O_2Se$[a]	0.063	—	—
$Bi_{1,96}Mn_{0,04}O_2Se$	0.076	—	—
$Bi_{1,9}Mn_{0,1}O_2Se$	—	—	0.446

[a] A very unreliable analysis.

substantial background concentration of electrons in the $x \leq 0.04$ samples is most likely due to V_{Se}.

Fig. 6 shows the Arrhenius analysis of excitation energies (levels) of $Bi_{2-x}Mn_xO_2Se$. The excitation energies are summarized in Table 3. In the undoped samples, two levels ($E_{a1} \approx 0.07$ eV and $E_{a2} \approx 0.20$ eV) can be found, the former is consistent with ref. 43. The lower is very weak and can be tentatively attributed to V_O. The higher is due to Se_{Bi} defects in accordance with ref. 30, consistent with our results (Fig. S4a and b). The Arrhenius analysis of the $x = 0.1$ sample shows one pure activation behavior with negligible background electron concentration, *i.e.* negligible concentration of active defects. The excitation with activation energy, $E_{a3} \cong 0.45$ eV, is due to the fundamental excitation over the band gap, $E_g \cong 0.90$ eV for the fundamental excitation (Fig. 6). This value is in agreement with the value of the indirect gap derived from ARPES measurements in the literature, $E_g \cong 0.8$ eV.[1] It is the first time that the thermal energy gap can be extracted from transport parameters.

The results of the experiments can be summarized as follows. The undoped samples are relatively rich in Se_{Bi} antisite defects which are accompanied by a lower concentration of and V_O and V_{Se}. Se_{Bi} and V_O show excitation at $E_{a1} \approx 0.075$ eV and at $E_{a2} \approx 0.21$ eV while V_{Se} defects form a background electron concentration due to zero activation energy, see DFT results and *e.g.* ref. 39. The concentration of all these defects decreases with the addition of Mn. Sample $x = 0.04$ still exhibits $E_{a1} \approx 0.075$ eV excitation, but sample $x = 0.1$ enters the intrinsic regime, showing only bandgap excitation with no states within the bandgap. To estimate the electron concentration, we measured the Hall effect on the undoped sample. The experiment (Fig. 7) shows a background electron concentration of about 3.7×10^{17} cm^{-3} at room temperature, which can be identified with the V_{Se} concentration. This concentration is much lower than that of the Mn_{Bi} acceptors in the $Bi_{1,9}Mn_{0,1}O_2Se$ sample, which explains the transition to p-type conductivity in this sample. Such a low vacancy concentration is not detectable in HRXRD experiments. It is worth noting that pair defects of V_{Se} and Mn_{Bi} ($Mn_{Bi} + V_{Se}$) lead to inactivation of selenium vacancies. Moreover, the formation of pair defects, O_{Se} and Mn_{Bi} ($Mn_{Bi} + O_{Se}$) also leads to the depletion of free V_{Se}. Both the pair defects have relatively low formation energy and behave as acceptors according to the DFT calculations (Table 2 and Fig. S4). Thus, there are three mechanisms leading to the n-type to p-type crossover. In addition to the acceptor-like nature of Mn_{Bi}, V_{Se} are depleted by the formation of ($Mn_{Bi} + O_{Se}$) and masked by the formation of complex defects ($Mn_{Bi} + V_{Se}$). For the Mn-doped samples, we could not perform the Hall measurement on polycrystalline samples due to their high resistivity. We have not yet been able to measure this value for single crystals from the same batch because Mn-doped single crystals are extremely fragile and also resistive. However, the phononic properties remain unchanged (Fig. S9).[32] In any case, the Hall experiments would be very difficult to evaluate due to the bipolar transport. We envisage that a proper doping (*e.g.* Mn-doping) can be used for formation of high permittivity ($\varepsilon_r \approx 500$)[32] gate insulators in integrated Bi_2O_2Se-based electronics. This is much higher value than that suggested for Bi_2SeO_5 ($\varepsilon_r \approx 25$).[6]

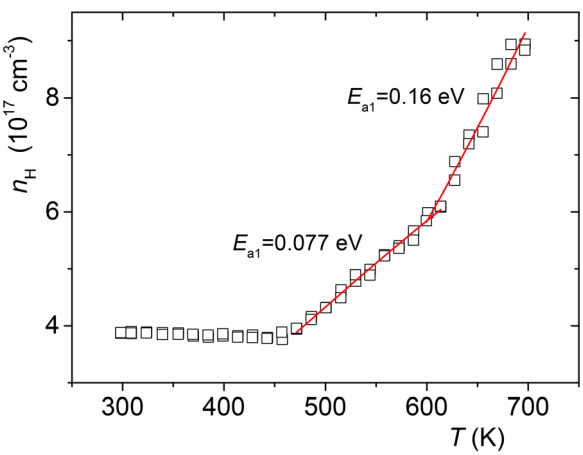

Fig. 7 Hall concentration as a function of temperature for the undoped Bi_2O_2Se (1) polycrystalline sample. RT background Hall electron concentration $n_H \approx 4 \times 10^{17}$ cm^{-3}. Two activation energies, $E_{a1} \approx 0.077$ eV and $E_{a2} \approx 0.16$ eV are derived by exponential fitting the T-dependence of Hall concentration (red lines). The experimental data represent temperature dependences in both directions.

4. Conclusion

In this paper, we report on Mn doped Bi_2O_2Se, $Bi_{2-x}Mn_xO_2Se$. Defect formation energies derived from DFT calculations suggest a spontaneous formation of Mn_{Bi} substitutional defects in contrast to experiments. EDS, HRXRD, and transport data indicate a very low solubility of Mn in the Bi_2O_2Se matrix while magnetic data confirm this conclusion. Analysis of magnetization and susceptibility data suggests formation of Mn^{2+} ions in a high spin configuration ($S_{spin} \approx 2.4$). The analysis gives a concentration of Mn^{2+} ions $N = 2.67 \times 10^{18}$ cm^{-3} and corresponding $x \cong 0.00025$ for the highest doping. Replacement of Bi by Mn leads to a decrease in the electron concentration mainly due to depletion/inactivation of the main native donors V_{Se}, and the formation of acceptors Mn_{Bi}. The DFT calculations suggest the acceptor-like pair defects ($Mn_{Bi} + V_{Se}$) and ($Mn_{Bi} + O_{Se}$), which mask the main donor, V_{Se}. The HRXRD analysis suggests a concentration of Se_{Bi} defects as high as $x \approx 0.07$ (3.5% of Bi sites) in undoped samples, but zero in Mn-doped samples. This is supported by EDS analysis which, however,

 © 2025 The Author(s). Published by the Royal Society of Chemistry

Open Access Article. Published on 08 September 2025. Downloaded on 3/3/2026 7:36:03 PM.
This article is licensed under a Creative Commons Attribution-NonCommercial 3.0 Unported Licence.

suggests much smaller non-stoichiometry. Transport measurements show a crossover from n-type to p-type conductivity with increasing Mn content consistent with the formation of Mn induced acceptors and depletion/inactivation of the main donors, V_{Se} and Se_{Bi}. The transport, EDS and HRXRD data are largely consistent with the DFT calculations. Thanks to Mn doping, p-type Bi_2O_2Se was prepared and the thermal bandgap energy E_g = 0.9 eV was determined for the first time.

Conflicts of interest

There are no conflicts to declare.

Data availability

The datasets supporting this article have been uploaded as part of the SI. See DOI: https://doi.org/10.1039/d5ma00543d.

Acknowledgements

The authors would like to thank the Czech Science Foundation for financial support (Project No. 22-05919S) and acknowledge the financial support from the grant of the Ministry of Education, Youth and Sports of Czech Republic (grant LM2023037).

References

1 J. Wu, H. Yuan, M. Meng, C. Chen, Y. Sun, Z. Chen, W. Dang, C. Tan, Y. Liu, J. Yin, Y. Zhou, S. Huang, H. Q. Xu, Y. Cui, H. Y. Hwang, Z. Liu, Y. Chen, B. Yan and H. Peng, *Nat. Nanotechnol.*, 2017, **12**, 530–534.
2 Q. Mao, X. Geng, J. Yang, J. Zhang, S. Zhu, Q. Yu, Y. Wang, H. Li, R. Li and H. Hao, *J. Cryst. Growth*, 2018, **498**, 244–247.
3 L. Xu, Y.-C. Luo, Y.-Y. Lv, Y.-Y. Zhang, Y.-Z. Wu, S.-H. Yao, J. Zhou, Y. B. Chen and Y.-F. Chen, *J. Phys.: Condens. Matter*, 2020, **32**, 365705.
4 J. Wang, W. Hu, Z. Lou, Z. Xu, X. Yang, T. Wang and X. Lin, *Appl. Phys. Lett.*, 2021, **119**, 081901.
5 C. Drasar, P. Ruleova, L. Benes and P. Lostak, *J. Electron. Mater.*, 2012, **41**, 2317–2321.
6 C. Zhang, T. Tu, J. Wang, Y. Zhu, C. Tan, L. Chen, M. Wu, R. Zhu, Y. Liu, H. Fu, J. Yu, Y. Zhang, X. Cong, X. Zhou, J. Zhao, T. Li, Z. Liao, X. Wu, K. Lai, B. Yan, P. Gao, Q. Huang, H. Xu, H. Hu, H. Liu, J. Yin and H. Peng, *Nat. Mater.*, 2023, **22**, 832–837.
7 T. Li and H. Peng, *Acc. Mater. Res.*, 2021, **2**, 842–853.
8 Z. Zhu, X. Yao, S. Zhao, X. Lin and W. Li, *J. Am. Chem. Soc.*, 2022, **144**, 4541–4549.
9 X. Ding, M. Li, P. Chen, Y. Zhao, M. Zhao, H. Leng, Y. Wang, S. Ali, F. Raziq, X. Wu, H. Xiao, X. Zu, Q. Wang, A. Vinu, J. Yi and L. Qiao, *Matter*, 2022, **5**, 4274–4314.
10 M. Li, P. Chen, Y. Zhao, M. Zhao, H. Leng, Y. Wang, S. Ali, F. Raziq, X. Wu, J. Yi, H. Xiao and L. Qiao, *InfoMat*, 2024, **6**, e12539.
11 N. Yang, L. Pan, C. Chen and Y. Wang, *J. Alloys Compd.*, 2021, **858**, 157748.
12 S. Y. Bae, H.-S. Kim, S. W. Lee, O. Park, H. Park and S. Kim, *J. Mater. Res. Technol.*, 2022, **19**, 2831–2836.
13 Z. Fu, J.-L. Jiang, S.-T. Dong, M.-C. Yu, L. Zhao, L. Wang and S.-H. Yao, *J. Mater. Res. Technol.*, 2022, **21**, 640–647.
14 L. Pan, Z. Zhao, N. Yang, W. Xing, J. Zhang, Y. Liu, C. Chen, D. Li and Y. Wang, *J. Eur. Ceram. Soc.*, 2020, **40**, 5543–5548.
15 X. Tan, J. Lan, K. Hu, B. Xu, Y. Liu, P. Zhang, X. Cao, Y. Zhu, W. Xu, Y. Lin and C. Nan, *J. Am. Ceram. Soc.*, 2018, **101**, 4634–4644.
16 X. Niu, Y. Gao, L. Pan, C. Chen and Y. Wang, *J. Alloys Compd.*, 2022, **921**, 166087.
17 C. Song, Y. Song, L. Pan, C. Chen, P. Zong and Y. Wang, *J. Alloys Compd.*, 2022, **892**, 162147.
18 H. Y. Hong, D. H. Kim, S. O. Won and K. Park, *J. Mater. Res. Technol.*, 2021, **15**, 4161–4172.
19 Y. Li, H. Huo, H. Huang, K. Guo, X. Yang, J. Xing, J. Luo, G.-H. Rao and J.-T. Zhao, *J. Mater. Sci.*, 2021, **56**, 12732–12739.
20 Y. Gao, Y. Wang, L. Pan, C. Chen, P. Zong and Y. Wang, *Mater. Lett.*, 2022, **308**, 131291.
21 X. Tan, J. Lan, G. Ren, Y. Liu, Y. Lin and C. Nan, *J. Am. Ceram. Soc.*, 2017, **100**, 1494–1501.
22 C. Song, H. Zhou, Y. Gu, L. Pan, C. Chen and Y. Wang, *J. Alloys Compd.*, 2023, **930**, 167439.
23 X. Tan, Y. Liu, R. Liu, Z. Zhou, C. Liu, J. Lan, Q. Zhang, Y. Lin and C. Nan, *Adv. Energy Mater.*, 2019, **9**, 1900354.
24 M. Kim, D. Park and J. Kim, *J. Alloys Compd.*, 2021, **851**, 156905.
25 P. Ruleova, T. Plechacek, J. Kasparova, M. Vlcek, L. Benes, P. Lostak and C. Drasar, *J. Electron. Mater.*, 2018, **47**, 1459–1466.
26 B. Zhan, S. Butt, Y. Liu, J.-L. Lan, C.-W. Nan and Y.-H. Lin, *J. Electroceramics*, 2015, **34**, 175–179.
27 B. Zhan, Y. Liu, J. Lan, C. Zeng, Y.-H. Lin and C.-W. Nan, *Materials*, 2015, **8**, 1568–1576.
28 L. Pan, X. Shi, C. Song, W. Liu, Q. Sun, C. Lu, Q. Liu, Y. Wang and Z. Chen, *Adv. Funct. Mater.*, 2022, **32**, 2202927.
29 A. Novitskii, M. Y. Toriyama, I. Serhiienko, T. Mori, G. J. Snyder and P. Gorai, *Adv. Funct. Mater.*, 2024, 2416509.
30 Q. Wei, C. Lin, Y. Li, X. Zhang, Q. Zhang, Q. Shen, Y. Cheng and W. Huang, *J. Appl. Phys.*, 2018, **124**, 055701.
31 H. Li, X. Xu, Y. Zhang, R. Gillen, L. Shi and J. Robertson, *Sci. Rep.*, 2018, **8**, 10920.
32 J. Zich, A. Sojka, P. Levinský, M. Míšek, K.-H. Ahn, J. Navrátil, J. Hejtmánek, K. Knížek, V. Holý, D. Nuzhnyy, F. Borodavka and S. Kamba, *Phys. Rev. Mater.*, 2025, **9**, 054603.
33 J. Zich, T. Plecháček, A. Sojka, P. Levinský, J. Navrátil, P. Ruleová, S. Šlang, K. Knížek, J. Hejtmánek, V. Nečina and Č. Drašar, *arXiv*, 2025, preprint, arXiv:2504.15227, DOI: 10.48550/arXiv.2504.15227.
34 P. Blaha, K. Schwarz, F. Tran, R. Laskowski, G. K. H. Madsen and L. D. Marks, *J. Chem. Phys.*, 2020, **152**, 074101.
35 F. Tran, P. Blaha and K. Schwarz, *J. Phys.: Condens. Matter*, 2007, **19**, 196208.
36 P. Schmidt, O. Rademacher, H. Oppermann and S. Däbritz, *Z. Anorg. Allg. Chem.*, 2000, **626**, 1999–2003.
37 X. Liu, D. Legut, R. Zhang, T. Wang, Y. Fan and Q. Zhang, *Phys. Rev. B*, 2019, **100**, 054438.

Open Access Article. Published on 08 September 2025. Downloaded on 3/3/2026 7:36:03 PM.
This article is licensed under a Creative Commons Attribution-NonCommercial 3.0 Unported Licence.

38 Q. Wei, R. Li, C. Lin, A. Han, A. Nie, Y. Li, L.-J. Li, Y. Cheng and W. Huang, *ACS Nano*, 2019, **13**, 13439–13444.
39 H. Fu, J. Wu, H. Peng and B. Yan, *Phys. Rev. B*, 2018, **97**, 241203.
40 Y.-Y. Lv, L. Xu, S.-T. Dong, Y.-C. Luo, Y.-Y. Zhang, Y. B. Chen, S.-H. Yao, J. Zhou, Y. Cui, S.-T. Zhang, M.-H. Lu and Y.-F. Chen, *Phys. Rev. B*, 2019, **99**, 195143.
41 T. Chattopadhyay, J. Rossat-Mignod and H. Fjellvåg, *Solid State Commun.*, 1987, **63**, 65–67.
42 G. Srinivasan and M. S. Seehra, *Phys. Rev. B: Condens. Matter Mater. Phys.*, 1983, **28**, 1–7.
43 Z. Xu, J. Wang, T. Wang, W. Hu, X. Yang and X. Lin, *Sci. China: Phys., Mech. Astron.*, 2021, **64**, 267312.

 © 2025 The Author(s). Published by the Royal Society of Chemistry